Astron. Astrophys. 330, 25–36 (1998)

ASTRONOMY AND ASTROPHYSICS

New bright soft X-ray selected ROSAT AGN

I. Infrared-to-X-ray spectral energy distributions⋆

D. Grupe[1,⋆⋆], K. Beuermann[1,2], H.-C. Thomas[3], K. Mannheim[1], and H.H. Fink[2,†]

[1] Universitäts-Sternwarte, Geismarlandstr. 11, D-37083 Göttingen, Germany
[2] MPI für extraterrestrische Physik, Giessenbachstr. 6, D-85748 Garching, Germany
[3] MPI für Astrophysik, Karl-Schwarzschildstr. 1, D-85748 Garching, Germany

Received 19 September 1996 / Accepted 9 September 1997

Abstract. We present results of an infrared-to-X-ray study of 76 bright soft X-ray selected Seyfert galaxies discovered in the ROSAT All-Sky Survey. These objects are characterized by steep X-ray spectra in the 0.2-2.0 keV bandpass with power law energy spectral indices in the range of 1.3 to 8 and a lack of internal absorption by neutral hydrogen. Our sample selection based on hardness ratio yields a mean slope of $\alpha_{\rm X} = 2.1 \pm 0.1$ ($F_\nu \propto \nu^{-\alpha}$), steeper than in any other known AGN population. At optical wavelengths, the soft AGN have significantly bluer spectra than a comparison sample of AGN with a canonical, harder X-ray spectrum, whereas the slope between 5500 Å and 1 keV is the same. This is consistent with a more pronounced Big Blue Bump emission component in the soft X-ray selected AGN. The blueness of the optical spectra increases with the softness of the X-ray spectra *and* with the luminosity, saturating at an approximate $F_\nu \propto \nu^{+0.3}$ spectrum. Such properties are expected if most of the Big Blue Bump emission originates in a (comptonized) accretion disk and $\dot{M}/M$ is higher than in AGN with a hard X-ray spectrum.

Key words: accretion, accretion disks – galaxies: active – galaxies: nuclei – quasars: general – galaxies: Seyfert

1. Introduction

The ROSAT All Sky Survey (RASS) has led to the discovery of a large number of X-ray sources (Voges et al. 1996, Voges 1997). Even among the brightest of these a sizable fraction coincides with objects not previously recognized as X-ray emitters. Of particular interest are those with very soft X-ray spectra because they are likely not to have been adequately covered by previous X-ray missions. Soft X-rays probe the high-energy accretion disk continuum and they are important for the photoionization of the nuclear gas in AGN. In this paper we discuss the infrared-to-X-ray continua of a high galactic latitude sample of the brightest soft X-ray selected AGN newly discovered in the RASS. This sample of 76 AGN is drawn from an optically identified sample of bright soft RASS sources (Thomas et al. in prep., Beuermann et al. in prep.).

In the $2-20$ keV energy range the X-ray spectra of AGN are characterized by a hard power-law with an energy spectral slope $\alpha_{\rm x} \sim 1.0$, perhaps lowered by a reflection component to $\alpha_{\rm x} \simeq 0.7$. Throughout this paper, spectral indices α are energy indices defined by $F_\nu \propto \nu^{-\alpha}$. Several recent studies demonstrated that the spectral index increases at photon energies below $\sim$ 1 keV (e.g. Walter & Fink 1993, Puchnarewicz et al. 1995a, Boller et al. 1996), indicating what appears to be a *soft X-ray excess* over an underlying hard power law component. In spite of an extensive debate there is no generally accepted explanation of the observed steepening of the X-ray spectra.

The presence of a soft excess was first noted by Arnaud et al. (1985) in the EXOSAT data of the Seyfert 1 galaxy Mkn 841. In the EINSTEIN era, Córdova et al. (1992) and Puchnarewicz et al. (1992) found that some serendipitously discovered AGN possessed "ultrasoft" X-ray spectra. Using RASS data, Walter & Fink (1993) showed that in a sample of 58 Sy1 galaxies the soft excess is part of a *Big Blue Bump* (henceforth BBB) which extends from the UV spectral range to soft X-ray energies. Because of the rapid spectral variability seen in many of these systems (e.g. Boller et al. 1993, 1996), the soft X-rays must originate from the innermost regions of the AGN. A popular interpretation of the BBB is thermal emission from an accretion disk (Shields 1978, Malkan & Sargent 1982, Malkan 1983, Band & Malkan, 1989), probably modified by comptonization which shifts some of the photons into the soft X-ray regime (Czerny & Elvis 1987, Laor & Netzer 1989, Ross et al. 1992, Mannheim et

Send offprint requests to: grupe@usw052.dnet.gwdg.de

⋆ Based in part on observations at the European Southern Observatory La Silla (Chile) with the 2.2m telescope of the Max-Planck-Society during MPG and ESO time, and the ESO 1.5m telescope

⋆⋆ Present address MPI für extraterestrische Physik, Garching, FRG; guest observer: McDonald Observatory, U of Texas at Austin.

† Deceased December 23, 1996.

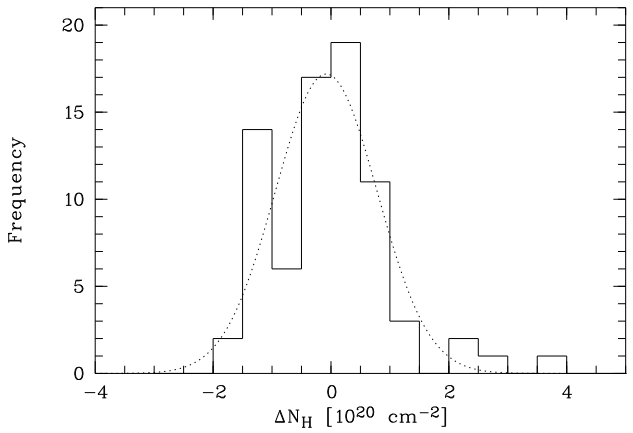

Fig. 1. Distribution of the difference $N_{\rm H}$-$N_{\rm H,gal}$ for our soft sample (solid histogram). The dotted line shows a Gaussian fit to this histogram with the center at -0.03 and σ = 0.87.

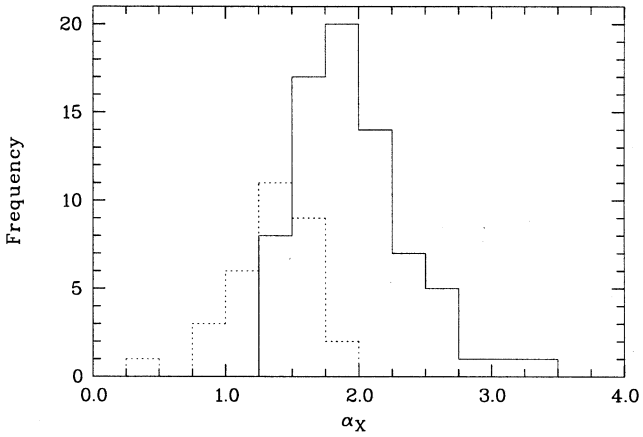

Fig. 2. Distributions of the single power law slopes $\alpha_{\rm x}$ of the unabsorbed X-ray spectra for the soft (solid) and hard sample (dotted). RX J0134 ($\alpha_{\rm x}$=6.7), RX J0136 (4.9), and WPVS007 (8.0) are off the plot.

al. 1995). Taking a different approach, Ferland & Rees (1988) and Guilbert & Rees (1988) suggested that hard X-ray emission is reprocessed into the optical-to-soft X-ray range by cold dense clouds, while Barvainis (1993) proposed that free-free emission from a high-temperature optically thin gas can account for the spectral shape of the BBB. A steep soft X-ray spectrum could also be produced by a warm absorber which preferentially absorbs X-rays at intermediate energies of $\sim 0.5 - 3$ keV, while being transparent at lower energies (George et al. 1995, Komossa & Fink 1997).

In this paper we present new data on ROSAT-discovered soft X-ray selected AGN from which we expect further clues on the origin of the soft X-rays and the nature of the BBB. In Sect. 2 we describe the X-ray observations and define the sample. The analysis of the X-ray data and the results of a correlation study between X-ray and optical continuum properties are presented in Sect. 3 and discussed in Sect. 4. All luminosities are calculated with $H_0 = 75\,{\rm km\,s^{-1}Mpc^{-1}}$ and $q_0 = \frac{1}{2}$. In a separate paper, we present the optical data and discuss correlations between optical and X-ray continuum properties and optical emission line properties (Grupe et al. in prep., hereafter Paper II).

2. Sample definition

The 76 sources presented in this paper were chosen from RASS data, observed with the Position Sensitive Proportional Counter (PSPC, Pfeffermann et al. 1986). Our optical identification program (Thomas et al. in prep., Beuermann et al. in prep.) focused on bright soft high galactic latitude sources fulfilling the criteria:

- galactic latitude $|\,b\,| > 20°$,
- PSPC count rate (CR) during the RASS $\gtrsim 0.5\,{\rm cts\,s^{-1}}$,
- hardness ratio HR1 + error (HR1)< 0, i.e. effectively more than 50% of the counts in the Carbon band ($E < 0.28$ keV).

The objects were chosen to be at high galactic latitudes to avoid cold absorption in the galactic plane. The high count rate was chosen for two reasons: first to get reasonable signal-to-noise ratios, and second to get better positions for reliable identifications. The hardness ratio is defined as HR1 = (HARD-SOFT)/(HARD+SOFT) where SOFT and HARD are the count rates in the energy bands $0.1 - 0.4$ and $0.4 - 2.4$ keV, respectively. HR1 is equivalent to an X-ray "colour".

All PSPC count rates quoted in this paper are from the RASS Bright Source Catalogue (RASS BSC) (Voges et al. 1997). The original source selection for our identification program was based on a limit of 0.5 cts s^{-1} in preliminary count rates which differ from those which finally entered the RASS BSC. As a consequence, our sample is not complete in terms of a flux limit.

The present sample includes 53 AGN which were previously unknown as X-ray as well a optical objects; it is supplemented by 23 objects which were known to be AGN in that an entry was found in the NASA/IPAC Extragalactic Database, but for which no optical spectra or only low-resolution spectra were available in the literature. Combined, we have a sample of 76 soft X-ray emitting AGN which were not previously known as X-ray sources and which had largely unknown optical spectroscopic properties. For most sources, we have taken flux-calibrated low-resolution identification spectra which cover the range from typically 3800 – 10000Å and, for the whole sample, we have collected medium-resolution ($\sim$ 5Å FWHM) optical spectroscopy, using telescopes at La Silla, the Observatoire de Haute-Provence, Calar Alto, and McDonald Observatory. In this paper, we make use of the low-resolution spectra which define the shape of the optical continuum; the emission-line properties will be discussed in Paper II.

In order to set the properties of the soft X-ray selected sample of AGN into perspective, we defined a comparison sample of hard X-ray selected sources (Grupe 1996)[1]. All of these have

[1] Fairall 009, Mkn 590, Mkn 1044, NGC 985, ESO 198-G24, 3C 120, Mkn 1095, Mkn 79, PG 0804+761, Mkn 704, Mkn 705, NGC 3783, Mkn 766, Mkn 205, ESO 383-G35, IC 4329A, Mkn 279, Mkn

PSPC count rates > 1 cts s^{-1} and hardness ratios HR1> 0 during the RASS. X-ray data of these sources were derived from the public ROSAT data archive at MPE Garching and optical data were taken from the literature. Because we included only well-known sources our comparison sample is also selected by optical criteria. Thus we miss any bright ROSAT-discovered hard X-ray AGN and might exclude AGN with high optical extinction.

3. Data analysis

For all X-ray reduction and analysis tasks we used the EXSAS data analysis package of the MPE Garching (Zimmermann et al. 1994). The X-ray spectra were derived from photon event tables covering the area of the sky around individual sources. Source counts were collected in a circle of 250 arcsec radius around the source position, and background counts from a circular region of 750 arcsec diameter with center offset 825 arcsec from the object position in the scan direction of the satellite and free of contaminating sources. Although the spectral fits extend nominally over the energy range $0.1 - 2.4$ keV, the number of counts below 0.2 keV and above 2.0 keV become very small, and the power law representation correspondingly uncertain. Unabsorbed fluxes and luminosities were, therefore, calculated for the restricted energy range of $0.2 - 2.0$ keV. Count rates CR and hardness ratios HR1 were derived along with the spectra and were generally found to be consistent with those given (later) in the RASS BSC (Voges et al. 1997). For consistency with published values we quote here CR and HR1 from the BSC.

Because of the limited signal-to-noise ratio of the RASS spectra we employed only single power law fits in the energy range $0.1 - 2.4$ keV with absorption by a column density $N_{\rm H}$ of cold material with solar abundances. The hydrogen column density was either taken equal to the galactic column density $N_{\rm H,gal}$ (Dickey & Lockman 1990) or left as a free parameter, $N_{\rm H,fit}$. As explained in Sect. 4.1, $N_{\rm H} = N_{\rm H,gal}$ is the appropriate choice for most of our objects.

The optical spectral index $\alpha_{\rm opt}$ is calculated from our low-resolution spectra (after subtraction of the FeII emission line complex, see Paper II), using the continuum flux densities at 4400Å and 7000Å. Comparing the spectral flux densities with CCD photometry in the BVR bands available for a subset of objects, we estimate uncertainties of $< 20\%$ in the absolute value of the visual flux and $\sim 10\%$ in the relative flux calibration between 4400 and 7000Å which translates into an error in $\alpha_{\rm opt}$ of about ± 0.4.

We have derived the mean overall energy distributions for the objects of the soft and the hard samples using the mean monochromatic luminosities νL_ν at selected wavelengths (henceforth abbreviated 'luminosities'). The IR luminosities for 71 of the sources at 12, 25, 60, and 100 μm were derived from the IRAS survey data using the ADDSCAN procedure of the Infrared Processing and Analysis Center (IPAC) at Caltech (the missing sources are in IRAS data gaps). Three-sigma upper limits are quoted if the signal strength is less than 3 σ of the rms fluctuations. Most sources are weak with exceptional cases exceeding 25 σ. The visual luminosities $\nu L_{\rm V}$ were determined from our optical spectra and CCD photometry. The X-ray luminosities at 250 eV and at 1 keV were calculated from the power law fits to the RASS spectra. All luminosities are in the rest-frame (assuming α = 1 in case of the IR data).

4. Results

Table 1 gives the redshift, the visual magnitude V, and the power law index $\alpha_{\rm opt}$ of the optical spectrum, and X-ray properties of the 76 AGN. The IR, optical and X-ray luminosities are given in Table 2 and the means and medians of the luminosities and spectral indices of the soft and hard samples are summarized in Table 3. Finally, Table 4 lists the correlations found among the continuum parameters of the soft X-ray sample.

4.1. X-ray spectra

In columns $6-8$ of Table 1, we list the exposure time, the mean RASS PSPC count rate CR and the hardness ratio HR1 from the RASS BSC (Voges et al. 1997). In columns $9-13$, we give the adopted column density of atomic hydrogen, the logarithm of the $0.2 - 2.0$ keV rest-frame energy flux, the energy spectral index $\alpha_{\rm x}$ of the best-fit power law, χ^2 for ν degrees of freedom, and $\Delta N_{\rm H} = N_{\rm H,fit} - N_{\rm H,gal}$. The uncertainty in $\log F_{\rm x}$ is determined mainly by the error in CR while the uncertainties in the monochromatic luminosities $L_{\rm 250eV}$ and $L_{\rm 1keV}$ depend mainly on the errors in CR and $\alpha_{\rm x}$ (and, of course, in H_0).

Fig. 1 shows the distribution of $\Delta N_{\rm H}$ for the present sample. The mean values of $N_{\rm H,fit}$ and $N_{\rm H,gal}$ coincide within the errors, $N_{\rm H,fit} = (1.62 \pm 0.11) \cdot 10^{20}$ cm^{-2} and $N_{\rm H,gal} = (1.67 \pm 0.08) \cdot 10^{20}$ cm^{-2}, i.e., the mean value of $\Delta N_{\rm H}$ is consistent with zero. The width of the distribution agrees with that expected from the errors of the spectral fits as given by the EXSAS program (Zimmermann et al. 1994). We conclude that there is no evidence for significant internal absorption in the majority of individual AGN of this sample. This is why we consider $N_{\rm H} = N_{\rm H,gal}$ and the resulting $\alpha_{\rm x}$ as the appropriate choice for most of our soft X-ray selected AGN. Only four sources have $\Delta N_{\rm H} > 2 \cdot 10^{20}$ cm^{-2} (RXJ0136-35, IC3599, RXJ2144-39, and MS2340-15) and for these we choose $N_{\rm H} = N_{\rm H,fit}$ with $\alpha_{\rm x}$ being derived from the free fit. Fig. 2 shows the corresponding distribution of the derived power law slopes for the soft X-ray sample along with those for the hard comparison sample. The values for RX J0136-35 and for the extremely soft transient sources WPVS007 (Grupe et al. 1995a) and RX J0134-42 (Mannheim et al. 1996) are off the plot. A final caveat is in place, because we do find some systematic dependence of the derived $\alpha_{\rm x}$ on $\Delta N_{\rm H}$, an effect which is most likely caused by the curvature of the steep X-ray spectra towards low energies, forming an excess over the power law at the higher energies. We will show in Sect. 5.2 that $\Delta N_{\rm H}$ can be used as a parameter to describe the soft X-ray excess. A

1383, Mkn 876, Mkn 506, EXO 1821+64, ESO 141-G55, Mkn 509, Mkn 1513, NGC 7213, NGC 7469, Mkn 926

Table 1. Parameters of the 76 AGN of the soft X-ray sample. The columns denote (1) running number, (2) the name of the object (full names are given in Table 2), (3) the redshift, (4) the visual continuum magnitude V (with estimated error ± 0.2 mag), (5) the optical spectral index $\alpha_{\rm opt}$ (with estimated error ± 0.4), (6) the exposure time in s, (7) the RASS PSPC count rate CR in cts s^{-1}, (8) the hardness ratio HR1, (9) the adopted atomic hydrogen column density in units of 10^{20}cm^{-2} (see footnote[3]), (10) the logarithm of the rest-frame $0.2-2.0$ keV energy flux in W m^{-2} for a power law spectrum with, (11) X-ray spectral index $\alpha_{\rm x}$(with errors from the fit, see EXSAS user's guide), (12) χ^2/ν for the fit, and (13) $\Delta N_{\rm H}$= $N_{\rm H,fit}$ $-N_{\rm H,gal}$ in the same units as (9) with errors from the X-ray spectral fit.

(1) No	(2) Name[1]	(3) z	(4) V	(5) $\alpha_{\rm opt}$	(6) $T_{\rm exp}$	(7) CR	(8) HR1	(9) $N_{\rm H}$	(10) log $F_{\rm x}$	(11) $\alpha_{\rm x}$	(12) χ^2/ν	(13) $\Delta N_{\rm H}$
1	RXJ0022-34	0.219	16.1	0.0	471	0.47±0.05	–0.33±0.07	1.39	–14.4	1.6±0.2	12/13	−0.4±1.3
2	ESO242-G8	0.059	16.1	1.4	345	0.50±0.04	–0.41±0.10	1.48	–14.2	1.6±0.2	14/12	−0.4±1.2
3	WPVS 007	0.029	14.8	0.6	268	0.98±0.08	–0.94±0.06	2.82	–14.2	8.0±2.0	10/13	−1.4±2.2
4	RXJ0057–22	0.062	14.5	0.4	509	2.72±0.10	–0.50±0.03	1.48	–13.7	1.9±0.1	23/29	+0.0±0.5
5	QSO0056–36	0.165	15.1	–0.3	704	0.65±0.03	–0.24±0.07	1.94	–14.1	1.7±0.2	10/9	−0.2±1.1
6	RXJ0100–51	0.062	15.4	1.0	306	1.04±0.08	–0.15±0.06	2.42	–13.9	1.7±0.2	9/18	−0.2±1.5
7	MS0117–28	0.349	16.0	0.0	721	0.32±0.02	–0.56±0.08	1.65	–14.3	2.4±0.3	14/17	−0.4±1.0
8	IRAS01267	0.093	15.4	0.4	251	0.96±0.08	–0.40±0.07	1.28	–14.2	1.6±0.2	22/15	+0.1±1.4
9	RXJ0134–42[2]	0.237	16.0	–0.1	574	0.21±0.05	–0.84±0.05	1.59	–14.9	6.7±2.6	2.2/6	−1.3±1.1
10	RXJ0136–35	0.289	18.0	0.9	539	0.50±0.05	–0.72±0.05	5.60[3]	–13.3	4.9±0.5[3]	14/16	+3.8±4.0
11	RXJ0148–27	0.121	15.5	0.6	415	2.42±0.10	–0.53±0.03	1.50	–13.8	2.0±0.1	26/20	+0.7±0.8
12	RXJ0152–23	0.113	15.6	0.5	702	1.06±0.07	–0.47±0.04	1.10	–14.2	1.6±0.1	11/15	+0.3±0.7
13	RXJ0204–51	0.151	16.6	0.7	489	0.43±0.06	–0.22±0.08	3.76	–14.1	2.3±0.3	11/12	−1.5±2.0
14	RXJ0228–40	0.494	15.2	0.0	748	0.57±0.06	–0.55±0.05	1.78	–14.2	2.1±0.2	9.4/9	+0.0±1.2
15	RXJ0319–26	0.079	15.9	1.3	263	0.52±0.06	–0.41±0.09	1.32	–14.5	2.0±0.3	8.9/8	−0.7±1.2
16	RXJ0323–49	0.071	16.5	1.5	845	1.48±0.06	–0.44±0.03	1.72	–13.9	2.0±0.1	29/26	+0.3±0.7
17	ESO301–G13	0.064	15.5	1.3	898	0.81±0.03	–0.37±0.05	2.19	–14.0	2.1±0.1	19/14	−0.4±0.9
18	VCV0331–37	0.064	16.3	1.1	353	0.59±0.04	–0.34±0.09	1.63	–14.3	1.6±0.3	11/9	+0.4±2.1
19	RXJ0349–47[2]	0.299	16.8	1.9	449	0.48±0.06	–0.69±0.06	1.44	–14.5	2.9±0.5	10/12	−0.2±1.1
20	Fairall 1116	0.059	15.2	0.9	222	1.49±0.09	–0.29±0.08	3.84	–13.5	2.4±0.2	21/20	−1.1±1.8
21	RXJ0412–47	0.132	15.9	1.0	163	0.78±0.10	–0.45±0.09	1.42	–14.3	1.8±0.3	3.7/7	−0.7±1.3
22	RXJ0426–57	0.104	14.1	0.0	797	3.63±0.09	–0.48±0.02	2.25	–13.4	2.2±0.1	68/30	−1.2±0.3
23	Fairall 303	0.040	16.2	1.1	384	0.66±0.05	–0.55±0.08	0.99	–14.2	1.6±0.2	12/20	+0.3±0.9
24	RXJ0435–46	0.070	17.1	1.5	652	0.37±0.05	–0.57±0.06	1.80	–14.6	2.2±0.3	22/13	−1.3±0.8
25	RXJ0435–36	0.141	17.1	1.8	471	0.45±0.06	–0.26±0.07	1.49	–14.5	1.6±0.2	12/12	−0.7±1.1
26	RXJ0437–47	0.052	15.3	0.2	649	1.08±0.07	–0.50±0.04	1.69	–14.1	2.0±0.2	17/14	−1.0±0.5
27	RXJ0438–61	0.069	15.7	0.4	2124	0.59±0.04	–0.14±0.03	2.93	–14.1	1.9±0.1	26/25	−1.1±0.7
28	RXJ0439–45	0.224	16.6	0.4	632	0.41±0.05	–0.77±0.04	2.05	–14.4	3.3±0.7	17/13	−1.3±0.9
29	RXJ0454–48[2]	0.363	17.7	0.4	452	0.11±0.05	–0.62±0.11	1.91	–14.9	2.4±0.7	0.9/2	+0.6±5.9
30	RXJ1005+43	0.178	16.4	0.1[4]	694	0.76±0.05	–0.58±0.04	1.08	–14.3	1.9±0.2	15/11	+0.6±0.9
31	CBS 126	0.079	15.4	0.7	853	1.22±0.04	–0.33±0.04	1.41	–14.0	1.6±0.1	28/20	−0.0±0.6
32	RXJ1014+46[2]	0.324	17.1	1.5[5]	715	0.19±0.05	–0.67±0.08	0.93	–15.0	2.0±0.5	5.0/6	+1.1±2.7
33	RXJ1017+29	0.049	15.7	1.6[4]	498	0.39±0.05	–0.31±0.08	2.61	–14.4	2.0±0.2	7.3/12	+0.2±2.4
34	Mkn 141	0.042	15.1	1.5	975	0.43±0.02	–0.38±0.07	1.07	–14.5	1.5±0.2	22/18	+0.2±1.2
35	Mkn 142	0.045	15.2	1.2	1034	0.98±0.03	–0.53±0.04	1.18	–14.0	1.8±0.1	31/25	+0.5±0.6
36	RXJ1050+55	0.333	16.7	1.5[5]	804	0.41±0.05	–0.75±0.04	0.63	–14.7	1.9±0.3	16/16	+0.4±0.9
37	EXO1055+60	0.149	16.9	1.3[4]	874	0.43±0.05	–0.70±0.04	0.60	–14.8	1.9±0.3	14/19	−0.2±0.6
38	RXJ1117+65	0.147	16.4	1.2	897	0.59±0.05	–0.66±0.04	0.91	–14.5	1.9±0.2	7.9/10	+0.8±1.0
39	Ton 1388	0.177	14.4	0.6	466	0.96±0.07	–0.46±0.05	1.22	–14.2	1.7±0.2	10/9	+0.2±0.9
40	Mkn 734	0.033	14.4	0.9	807	0.37±0.02	–0.28±0.08	2.64	–14.3	2.0±0.2	16/14	−1.3±1.2
41	Z1136+34	0.033	16.0	1.6[4]	591	0.42±0.03	–0.30±0.09	2.04	–14.2	1.9±0.2	10/18	−0.4±1.2
42	CSO 109	0.059	16.3	1.4[4]	863	0.38±0.02	–0.30±0.08	1.96	–14.4	1.7±0.2	22/16	+1.2±2.2
43	RXJ1231+70	0.208	16.0	1.6[5]	1054	1.05±0.05	–0.14±0.03	1.67	–14.0	1.4±0.1	21/23	+0.2±0.7
44	IC 3599	0.021	16.5	1.8	670	4.91±0.11	–0.55±0.02	3.77[3]	–13.1	3.2±0.1[3]	70/42	+2.7±0.8
45	IRAS1239+33	0.044	15.1	2.4[4]	529	1.08±0.06	–0.08±0.05	1.35	–14.2	1.3±0.1	16/12	+0.7±1.2
46	RXJ1312+26	0.061	16.2	1.4[4]	694	0.57±0.05	–0.45±0.05	1.10	–14.5	1.5±0.2	17/20	−0.1±0.9
47	RXJ1314+34	0.075	16.3	0.8	758	0.70±0.05	–0.54±0.04	0.99	–14.5	2.0±0.2	21/11	+0.7±1.0
48	RXJ1355+56	0.122	16.5	1.7[4]	842	0.71±0.06	–0.56±0.06	1.15	–14.4	1.9±0.2	13/12	+0.8±1.0
49	RXJ1413+70	0.107	16.9	2.9[4]	1028	0.83±0.05	–0.16±0.05	1.93	–14.1	1.5±0.1	18/17	−0.8±0.7
50	Mkn 684	0.046	14.7	1.2	810	0.51±0.03	–0.17±0.07	1.50	–14.4	1.4±0.2	20/18	+0.4±1.4

Table 1. (continued)

(1) No	(2) Name[1)]	(3) z	(4) V	(5) α_{opt}	(6) T_{exp}	(7) CR	(8) HR1	(9) N_H	(10) $\log F_x$	(11) α_x	(12) χ^2/ν	(13) ΔN_H
51	Mkn 478	0.077	14.6	0.7	926	2.98±0.06	–0.65±0.02	1.04	–13.6	2.1±0.1	35/33	+0.2±0.3
52	RXJ1618+36	0.034	16.6	1.6[4]	1140	0.86±0.05	–0.36±0.03	1.26	–14.2	1.5±0.1	12/19	+0.0±0.6
53	RXJ1646+39	0.100	17.1	1.3[4]	4086	0.43±0.01	–0.40±0.03	1.40	–14.5	1.6±0.2	22/17	+0.7±1.5
54	RXJ2144–39	0.140	18.0	1.2	496	0.43±0.05	–0.42±0.07	4.89[3)]	–13.8	3.4±0.3[3)]	12/11	+2.5±3.7
55	RXJ2154–44	0.344	15.8	0.2	521	0.46±0.05	–0.64±0.06	2.07	–14.3	2.5±0.4	16/12	−1.4±0.8
56	RXJ2213–17	0.146	17.2	1.1	373	0.49±0.06	–0.57±0.07	2.48	–14.3	2.4±0.4	13/11	−1.8±0.9
57	RXJ2216–44	0.136	15.8	0.2	486	1.45±0.08	–0.61±0.03	2.17	–13.9	2.5±0.2	24/15	−1.3±0.5
58	RXJ2217–59	0.160	16.2	0.3	603	0.81±0.06	–0.60±0.04	2.58	–14.0	2.7±0.2	8.9/10	−1.1±0.9
59	RXJ2221–27[2)]	0.177	17.7	0.5	417	0.29±0.06	–0.60±0.08	1.42	–14.7	2.1±0.4	5.0/7	−0.8±1.2
60	RXJ2232–41[2)]	0.075	16.9	0.9	442	0.22±0.05	–0.48±0.10	1.60	–14.8	1.8±0.5	8.6/5	−0.4±2.1
61	RXJ2241–44	0.545	15.8	0.3	467	0.40±0.05	–0.68±0.06	1.76	–14.3	2.5±0.4	14/10	−0.4±1.4
62	RXJ2242–38	0.221	16.9	1.0	454	0.66±0.06	–0.58±0.05	1.18	–14.4	2.2±0.3	14/15	+0.7±1.4
63	RXJ2245–46	0.201	14.8	0.8	477	1.65±0.08	–0.64±0.03	1.95	–13.8	2.5±0.2	39/14	−1.3±0.4
64	RXJ2248–51	0.102	15.5	1.3	503	2.62±0.13	–0.54±0.03	1.27	–13.8	1.9±0.1	15/25	−0.5±0.4
65	MS2254–37	0.039	15.0	1.9	369	1.19±0.06	–0.52±0.06	1.15	–14.0	1.8±0.1	33/13	+0.3±0.8
66	RXJ2258–26	0.076	16.1	1.3	145	0.69±0.09	–0.11±0.12	2.11	–14.1	1.5±0.3	3.7/6	+1.3±3.8
67	RXJ2301–55	0.140	15.4	0.1	567	0.88±0.07	–0.54±0.04	1.54	–14.2	2.1±0.2	6.6/10	+0.0±0.8
68	RXJ2303–55	0.084	17.5	1.9	527	0.35±0.05	–0.21±0.08	1.54	–14.5	1.4±0.2	13/10	+0.2±1.9
69	RXJ2304-35	0.042	16.6	1.4	205	0.56±0.07	–0.37±0.10	1.47	–14.4	1.5±0.1	3.7/6	−0.2±2.0
70	RXJ2304-51	0.106	17.2	1.1	418	0.38±0.06	–0.40±0.09	1.33	–14.6	1.8±0.3	4.3/9	−0.3±1.4
71	RXJ2317–44[2)]	0.134	16.8	0.3	270	0.73±0.08	–0.74±0.05	1.89	–14.3	2.6±0.4	14/11	−0.9±1.1
72	RXJ2325–32	0.216	17.0	0.8	130	0.58±0.09	–0.58±0.11	1.33	–14.4	2.1±0.5	5.0/4	+0.5±3.2
73	RXJ2340–53[2)]	0.321	17.6	0.1	231	0.29±0.06	–0.71±0.10	1.81	–14.5	2.1±0.6	9.4/3	−1.1±2.0
74	MS2340–15	0.137	15.6	0.8	457	0.74±0.06	–0.39±0.06	4.36[3)]	–13.7	3.2±0.2[3)]	17/16	+2.2±2.5
75	RXJ2349–33	0.135	16.6	1.3	491	0.49±0.05	–0.49±0.07	1.04	–14.5	1.6±0.2	7.7/13	+0.9±1.7
76	RXJ2349-31	0.135	16.6	1.6	462	0.60±0.06	–0.45±0.06	1.23	–14.4	1.6±0.2	15/16	−0.0±1.1

[1)] Exact coordinates of the new sources will be given in paper II
[2)] These sources have original count rates below the limit that defined the sample.
[3)] $N_H = N_{H,fit}$ and α_x from $N_{H,fit}$; for all others $N_H = N_{H,gal}$ and α_x from $N_{H,gal}$
[4)] α_{opt} determined from the 1994 McDonald spectra covering 1400 Å only
[5)] Same, but additional uncertainty due to the larger redshifts (not included in Figs. 6 and 7)

more detailed analysis would require better X-ray spectra than obtained from the RASS.

4.2. Overall energy distributions

The luminosities of each individual source are given in Table 2. The mean luminosities are listed in Table 3 and plotted in Fig. 3. The optical reference wavelength is 5500 Å, the soft and hard X-ray reference energies are 250 eV and 1 keV, respectively. The mean IR-luminosities of the soft sample were calculated by a Kaplan-Meier estimator (see Babu & Feigelson 1996) which allows to take the upper limits into account. The visual and hard X-ray luminosities of both samples happen to agree (Table 3 and Fig. 3), whereas the soft X-ray and IR-luminosities of the soft AGN exceed those of the hard comparison sample.

Also given in Table 3 are α_{opt} and α_x along with several two-point spectral indices, connecting different spectral regions. The mean α_x of our soft sample (2.11±0.10) agrees with that of the optically selected NLSy1 sample of Boller et al. (1996) (weighted mean $\alpha_x = 2.13 \pm 0.03$). The mean α_x of the hard comparison sample (1.35±0.06), on the other hand, agrees reasonably well with the corresponding values for the optically selected Sy1 sample of Walter & Fink (1993), 1.50 ± 0.07 (with standard error quoted), and the IR selected sample of Rush et al. (1996), 1.26±0.11. Laor et al. (1997) obtain $\alpha_x = 1.63 \pm 0.09$ for a sample of optically selected quasars.

The soft and hard samples have the same mean optical to hard X-ray slopes $\alpha_{ox-hard}$. They differ in their X-ray spectral indices α_x, optical spectral indices α_{opt}, and optical-to-soft X-ray spectral indices $\alpha_{ox-soft}$. The infrared spectral indices are only marginally different (see Fig. 3).

Fig. 4 displays the spectra of three NLSy1 galaxies which bracket the α_x vs. L_{250eV} correlation shown in Fig. 6. Obviously, there exists a large diversity of the spectral shapes of individual sources. As a general trend, however, the BBB becomes more pronounced at higher luminosities.

Fig. 5 displays the distributions of the visual luminosities νL_V of the soft and hard sample. The falloff towards high luminosities represents the local luminosity function, the falloff towards low luminosities is produced by our cutoff in PSPC

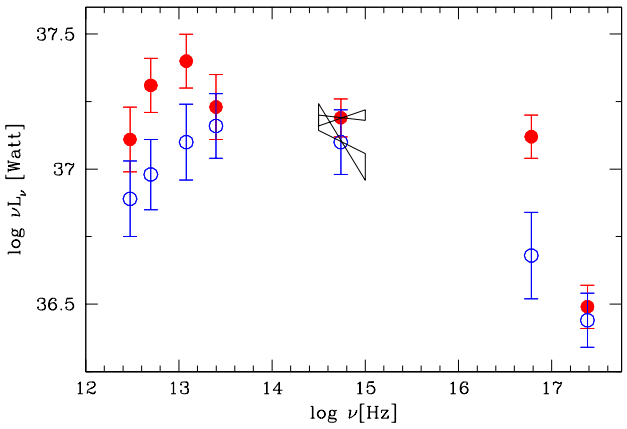

Fig. 3. Spectral energy distributions of soft X-ray (*solid circles*) and hard X-ray (*open circles*) selected AGN, respectively. Error bars represent the standard errors of the mean.

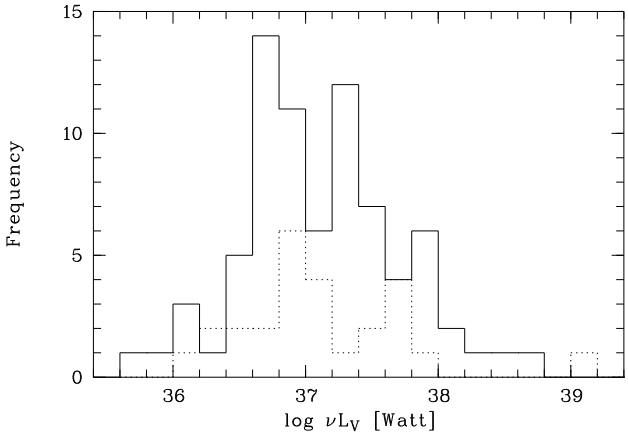

Fig. 5. Distributions of the optical monochromatic rest-frame luminosities νL_V at 5500 Å for the soft (solid) and hard sample (dotted).

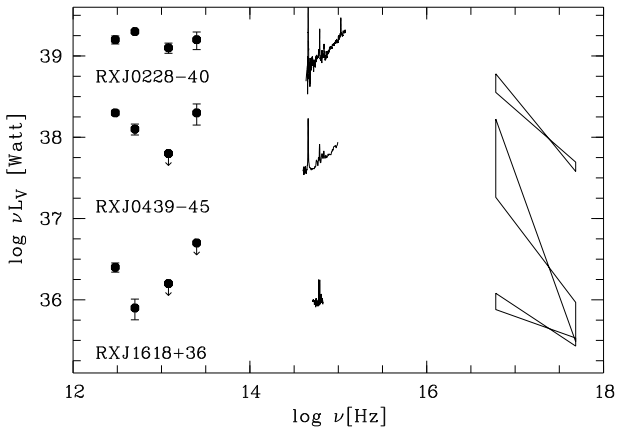

Fig. 4. Examples of (rest-frame) spectral energy distributions of soft X-ray selected NLSy1 galaxies. Arrows indicate 3-σ upper limits.

count rate. As a consequence, our sample is biased in luminosity and in α_x, by virtue of the hardness ratio cut which removes most sources with canonical Seyfert X-ray spectra.

4.3. Correlations

Correlations between the various monochromatic luminosities and two-point spectral indices were studied employing the Spearman rank-order test. The results are given in Table 4.

Fig. 6 shows α_{opt} and α_x vs. L_{250eV}. The optical index α_{opt} displays a clear variation with luminosity in the sense that the spectrum becomes bluer with increasing 250 eV luminosity[2]. The significance of this anti-correlation is high ($t = -5.3$, see Table 4). The spectral energy distributions of AGN of low and high luminosity are considerably different as demonstrated in Fig. 4. Since L_V correlates with L_{250eV} (t = 14.0), the correlations between the spectral indices and L_V are similarly significant, see Table 4. Furthermore, for $\alpha_x \simeq 2$, $L_x(0.2-2\,\mathrm{keV})$ is mainly dependent on the spectral flux at low energies, hence, L_{250eV}. The correlations between α_x and the luminosities and the anti-correlations between α_{opt} vs. luminosities imply an anti-correlation between both spectral indices, if the relation is real. Spearman's rank order test indeed reveals a convincing anti-correlation at a significance level of $t = -3.9$ (Table 4). We will see below that ΔN_H appears to be related to a soft X-ray excess showing a weaker correlation with the optical spectral slope (t = 3.1).

Although α_{opt} could be influenced by the continuum of the host galaxy, we see no spectral features indicative of the host galaxy. The nuclear property α_x also shows a systematic variation with L_{250eV} at the significance level of t = 6.7. Cold, dusty gas might be expected to steepen the optical continuum and depress the soft X-rays, producing a correlation between α_{opt} and α_x in the sense that we observe. However, a neutral hydrogen column of 10^{20} cm^{-2}, corresponding to $E_{B-V} \sim 0.02$, would produce a change of only 0.08 in α_{opt}, so absorption by cold, dusty gas is not the cause of the correlation. This is further supported by a lack of any correlation between α_x and the Hα/Hβ intensity ratio (Paper II, Grupe et al. 1997). We are aware that a warm dusty absorber could redden the optical continuum without affecting the Balmer decrement. However, as pointed out in Sect. 4.3, a warm absorber would tend to *steepen* the X-ray spectrum, contrary to what is required to explain the anti-correlation between α_{opt} and α_x. A selection effect is not responsible for the lack of low-luminosity, steep-spectrum X-ray sources. Redshift effects are unimportant, since the average redshift is only z = 0.14 (Table 2) (e.g. Schartel et al. 1996).

The observation that $\alpha_{ox-hard}$ remains constant independent of α_x, whereas $\alpha_{ox-soft}$ becomes flatter for the steeper X-ray spectra (Fig. 7) is suggestive of an underlying spectrum which connects optical and 1 keV fluxes. The slope of this steep-spectrum continuum component is 1.3 for soft *and* hard X-ray

[2] A similar result was previously reported by Barvainis (1993) for the soft X-ray sample of Puchnarewicz et al. (1992) which suffered, however, from problems in the processing of the EINSTEIN IPC data (see Thompson et al. 1994).

Table 2. Logarithms of monochromatic rest-frame luminosities νL_ν $[W]$ for the soft X-ray selected AGN listed in Table 1. Missing IR luminosities are due to IRAS data gaps. The upper limits denote fluxes less than 3-σ of the rms fluctuations.

No.	Name	$\nu L_{100\mu}$	$\nu L_{60\mu}$	$\nu L_{25\mu}$	$\nu L_{12\mu}$	$\nu L_{\rm V}$	$\nu L^{1)}_{250{\rm eV}}$	$\nu L^{1)}_{1{\rm keV}}$
1	RX J0022.5–3407	$38.7^{+.04}_{-.05}$	$38.5^{+.04}_{-.05}$	<38.3	<38.3	37.7	37.5	$37.1^{+.11}_{-.15}$
2	ESO 242-G8	<37.0	$37.1^{+.10}_{-.14}$	$37.1^{+.07}_{-.08}$	<37.2	36.6	36.5	$36.1^{+.11}_{-.14}$
3	WPVS 007	—	—	—	—	36.5	$36.2^{+.15}_{-.24}$	32.0
4	RX J0057.3–2222	<36.7	$36.9^{+.09}_{-.10}$	$37.8^{+.03}_{-.03}$	$37.3^{+.12}_{-.16}$	37.3	37.1	$36.6^{+.05}_{-.06}$
5	QSO0056–363	<37.8	$37.9^{+.05}_{-.06}$	<37.9	<38.2	37.9	37.5	$37.1^{+.07}_{-.08}$
6	RX J0100.4–5113	$37.4^{+.06}_{-.06}$	$37.2^{+.04}_{-.04}$	$37.4^{+.03}_{-.04}$	<37.2	36.9	36.8	$36.4^{+.08}_{-.10}$
7	MS 0117.2–2837	<38.5	<38.5	$38.7^{+.11}_{-.15}$	<38.9	38.2	38.3	$37.4^{+.13}_{-.20}$
8	IRAS 01267–2157	$37.4^{+.10}_{-.13}$	$37.7^{+.13}_{-.18}$	$37.7^{+.06}_{-.07}$	$37.4^{+.02}_{-.02}$	37.3	36.9	$36.5^{+.10}_{-.13}$
9	RX J0134.2–4258	<38.2	$37.9^{+.10}_{-.12}$	<38.1	<38.3	37.9	$37.5^{+.26}_{-.75}$	34.0
10	RX J0136.9–3510	<38.3	<38.1	$38.5^{+.09}_{-.11}$	<38.7	37.4	39.2	$36.9^{+.19}_{-.35}$
11	RX J0148.3–2758	<37.5	$37.3^{+.12}_{-.16}$	$38.0^{+.05}_{-.05}$	$37.9^{+.10}_{-.13}$	37.5	37.7	$37.1^{+.06}_{-.07}$
12	RX J0152.4–2319	$37.7^{+.06}_{-.07}$	$37.5^{+.08}_{-.09}$	$37.9^{+.06}_{-.07}$	$38.3^{+.04}_{-.04}$	37.4	37.1	$36.7^{+.06}_{-.08}$
13	RX J0204.0–5104	<37.3	<37.4	<37.5	<37.9	37.3	37.6	$36.8^{+.11}_{-.15}$
14	RX J0228.2–4057	$39.2^{+.05}_{-.05}$	$39.3^{+.02}_{-.02}$	$39.1^{+.06}_{-.07}$	$39.2^{+.10}_{-.12}$	38.9	38.7	$38.0^{+.10}_{-.12}$
15	RX J0319.8–2627	$37.2^{+.09}_{-.12}$	$37.4^{+.05}_{-.05}$	$37.2^{+.08}_{-.10}$	<37.5	37.0	36.5	$35.9^{+.17}_{-.20}$
16	RX J0323.2–4931	<36.9	$37.0^{+.06}_{-.07}$	$36.9^{+.10}_{-.15}$	<37.3	36.7	37.0	$36.4^{+.05}_{-.06}$
17	ESO 301-G13	$37.2^{+.06}_{-.07}$	$37.2^{+.03}_{-.03}$	$37.5^{+.03}_{-.04}$	<37.2	36.9	36.9	$36.2^{+.07}_{-.11}$
18	VCV0331-373	$36.9^{+.06}_{-.07}$	<36.8	<37.0	<37.2	36.6	36.5	$36.1^{+.12}_{-.17}$
19	RX J0349.1–4711	$38.3^{+.07}_{-.08}$	$38.3^{+.07}_{-.08}$	$38.7^{+.04}_{-.05}$	<38.7	37.9	38.0	$36.9^{+.23}_{-.52}$
20	Fairall 1116	$35.8^{+.11}_{-.15}$	$36.7^{+.08}_{-.10}$	$36.9^{+.10}_{-.13}$	$37.3^{+.07}_{-.08}$	37.0	37.4	$36.5^{+.09}_{-.11}$
21	RX J0412.7–4712	$37.5^{+.09}_{-.12}$	$37.8^{+.03}_{-.04}$	<37.4	$37.7^{+.12}_{-.17}$	37.5	37.2	$36.7^{+.16}_{-.25}$
22	RX J0426.0–5112	<37.2	$37.3^{+.05}_{-.06}$	$37.5^{+.05}_{-.05}$	$37.7^{+.10}_{-.13}$	37.9	37.9	$37.2^{+.04}_{-.04}$
23	Fairall 303	<36.4	$36.6^{+.05}_{-.06}$	$36.6^{+.06}_{-.07}$	<36.7	36.2	36.2	$35.8^{+.09}_{-.11}$
24	RX J0435.2–4615	<36.9	$37.0^{+.06}_{-.06}$	<36.9	$37.6^{+.05}_{-.06}$	36.4	36.4	$35.7^{+.14}_{-.21}$
25	RX J0435.9–3636	<37.6	$37.4^{+.12}_{-.17}$	<37.8	<37.9	37.0	37.0	$36.7^{+.11}_{-.14}$
26	RX J0437.4–4711	$36.9^{+.06}_{-.07}$	<36.6	<36.6	<36.9	36.9	36.6	$36.0^{+.08}_{-.09}$
27	RX J0438.5–6148	<36.9	$36.9^{+.04}_{-.04}$	$37.0^{+.12}_{-.17}$	$37.8^{+.03}_{-.04}$	36.9	36.8	$36.3^{+.04}_{-.04}$
28	RX J0439.7–4540	$38.3^{+.03}_{-.03}$	$38.1^{+.06}_{-.07}$	<37.8	$38.3^{+.11}_{-.15}$	37.7	$37.8^{+.06}_{-.07}$	36.4
29	RX J0454.7–4813	<38.3	$38.7^{+.03}_{-.03}$	<38.4	<38.8	37.6	$37.7^{+.13}_{-.18}$	36.8
30	RX J1005.7+4332	$38.2^{+.06}_{-.07}$	$38.4^{+.02}_{-.02}$	$38.2^{+.06}_{-.06}$	<38.1	37.4	37.4	$36.9^{+.09}_{-.10}$
31	CBS 126	<37.2	<37.0	<37.2	<37.3	37.1	37.0	$36.6^{+.05}_{-.06}$
32	RX J1014.0+4619	<38.3	<38.1	$38.8^{+.05}_{-.06}$	<38.7	37.9	37.4	$36.8^{+.23}_{-.36}$
33	RX J1017.3+2914	$37.0^{+.05}_{-.05}$	$37.0^{+.04}_{-.04}$	$37.1^{+.05}_{-.06}$	<37.0	36.6	36.3	$35.7^{+.11}_{-.14}$
34	Mkn 141	$37.4^{+.02}_{-.02}$	$37.5^{+.01}_{-.01}$	$37.2^{+.03}_{-.03}$	$37.5^{+.03}_{-.04}$	36.7	35.9	$35.6^{+.09}_{-.12}$
35	Mkn 142	$36.8^{+.09}_{-.11}$	$36.6^{+.11}_{-.15}$	$36.6^{+.12}_{-.17}$	<36.9	36.7	36.5	$36.0^{+.05}_{-.06}$
36	RX J1050.9+5527	$38.8^{+.04}_{-.04}$	$38.7^{+.04}_{-.04}$	$38.6^{+.05}_{-.06}$	<39.1	38.0	37.7	$37.1^{+.16}_{-.25}$
37	EXO 1055.3+6032	<37.6	$37.7^{+.06}_{-.07}$	<37.7	$38.0^{+.10}_{-.13}$	37.1	36.8	$36.3^{+.14}_{-.20}$
38	RX J1117.1+6522	$37.7^{+.12}_{-.16}$	$37.7^{+.07}_{-.08}$	$38.0^{+.05}_{-.06}$	$38.5^{+.04}_{-.05}$	37.3	37.1	$36.5^{+.10}_{-.12}$
39	Ton 1388	—	—	—	—	38.2	37.5	$37.1^{+.08}_{-.10}$
40	Mkn 734	$36.9^{+.04}_{-.04}$	$36.8^{+.03}_{-.03}$	$36.9^{+.08}_{-.10}$	$37.0^{+.09}_{-.12}$	36.7	36.0	$35.3^{+.10}_{-.13}$
41	Z 1136.6+3412	—	—	—	—	36.1	36.1	$35.6^{+.09}_{-.11}$
42	CSO 109	—	—	—	—	36.5	36.3	$35.9^{+.09}_{-.12}$
43	RX J1231.6+7044	$38.1^{+.08}_{-.10}$	$37.9^{+.08}_{-.10}$	$38.4^{+.04}_{-.04}$	<39.1	37.9	37.8	$37.5^{+.04}_{-.04}$
44	IC 3599	<36.0	$35.8^{+.07}_{-.08}$	<36.1	<36.3	35.6	37.0	$35.7^{+.05}_{-.06}$
45	IRAS 12397+3333	$36.8^{+.05}_{-.06}$	$37.1^{+.02}_{-.02}$	$37.4^{+.03}_{-.04}$	$37.0^{+.10}_{-.13}$	36.7	36.1	$35.9^{+.06}_{-.07}$
46	RX J1312.9+2628	<36.8	<36.8	$37.0^{+.09}_{-.11}$	<37.4	36.6	36.2	$35.9^{+.09}_{-.11}$
47	RX J1314.3+3429	<37.0	<37.0	<37.1	<37.6	36.7	36.5	$36.0^{+.09}_{-.12}$
48	RX J1355.2+5612	$37.5^{+.04}_{-.05}$	$37.1^{+.04}_{-.05}$	$37.9^{+.04}_{-.05}$	$37.2^{+.04}_{-.05}$	37.0	37.1	$36.5^{+.08}_{-.10}$
49	RX J1413.6+7029	$37.3^{+.12}_{-.17}$	$37.6^{+.05}_{-.06}$	<37.2	$37.6^{+.11}_{-.14}$	36.9	37.1	$36.8^{+.05}_{-.05}$
50	Mkn 684	$36.8^{+.08}_{-.09}$	$36.9^{+.05}_{-.05}$	$36.9^{+.05}_{-.05}$	$37.8^{+.01}_{-.01}$	36.9	36.0	$35.8^{+.08}_{-.09}$
51	Mkn 478	$37.5^{+.06}_{-.07}$	$37.6^{+.05}_{-.05}$	$37.2^{+.08}_{-.10}$	$37.5^{+.08}_{-.10}$	37.4	37.5	$36.8^{+.04}_{-.04}$
52	RX J1618.1+3619	$36.4^{+.05}_{-.06}$	$35.9^{+.11}_{-.15}$	<36.2	<36.7	35.9	36.0	$35.7^{+.05}_{-.06}$
53	RX J1646.4+3929	$37.4^{+.08}_{-.10}$	$37.3^{+.06}_{-.07}$	$37.5^{+.06}_{-.07}$	$37.6^{+.08}_{-.09}$	36.6	36.7	$36.3^{+.09}_{-.11}$
54	RX J2144.1–3949	$37.6^{+.07}_{-.12}$	$37.5^{+.10}_{-.12}$	<37.7	<38.0	36.7	38.0	$36.5^{+.18}_{-.33}$

Table 2. (continued)

No.	Name	$\nu L_{100\mu}$	$\nu L_{60\mu}$	$\nu L_{25\mu}$	$\nu L_{12\mu}$	$\nu L_{\rm V}$	$\nu L^{1)}_{250\rm eV}$	$\nu L^{1)}_{1\rm keV}$
55	RX J2154.1–4414	<38.6	<38.3	$38.9^{+.04}_{-.05}$	<38.7	38.3	38.3	$37.3^{+.18}_{-.31}$
56	RX J2213.0–1710	<37.5	$37.6^{+.08}_{-.10}$	$38.0^{+.08}_{-.10}$	<38.2	37.0	37.5	$36.6^{+.16}_{-.24}$
57	RX J2216.9–4451	<37.8	<37.4	$38.2^{+.04}_{-.05}$	$38.3^{+.03}_{-.03}$	37.4	37.8	$36.9^{+.09}_{-.11}$
58	RX J2217.9–5941	$38.7^{+.03}_{-.03}$	$38.5^{+.01}_{-.01}$	$38.2^{+.04}_{-.05}$	<38.3	37.4	37.8	$36.8^{+.11}_{-.14}$
59	RX J2221.8–2713	$37.9^{+.11}_{-.14}$	$37.7^{+.10}_{-.12}$	<38.0	<38.2	37.0	37.1	$36.5^{+.21}_{-.31}$
60	RX J2232.7–4134	<37.1	$36.9^{+.11}_{-.15}$	<37.3	$37.8^{+.05}_{-.05}$	36.5	36.2	$35.7^{+.20}_{-.29}$
61	RX J2241.8–4405	<39.0	<38.7	<38.8	$39.4^{+.08}_{-.09}$	38.8	38.7	$37.8^{+.20}_{-.37}$
62	RX J2242.6–3845	<38.1	<37.9	$38.2^{+.12}_{-.16}$	<38.4	37.5	37.6	$36.9^{+.14}_{-.21}$
63	RX J2245.3–4652	$38.2^{+.01}_{-.01}$	$38.4^{+.03}_{-.03}$	$38.2^{+.10}_{-.12}$	$38.7^{+.06}_{-.07}$	38.3	38.2	$37.3^{+.09}_{-.10}$
64	RX J2248.6–5109	$37.6^{+.07}_{-.09}$	$37.7^{+.03}_{-.03}$	$37.4^{+.11}_{-.15}$	<37.7	37.4	37.5	$36.9^{+.06}_{-.07}$
65	MS2254.9–3712	$36.8^{+.03}_{-.04}$	$36.9^{+.03}_{-.03}$	$36.8^{+.09}_{-.12}$	<37.1	36.7	36.4	$35.9^{+.08}_{-.10}$
66	RX J2258.7–2609	<37.1	<37.0	<37.4	<37.5	36.8	36.7	$36.5^{+.12}_{-.17}$
67	RX J2301.8–5508	$38.0^{+.06}_{-.07}$	$38.0^{+.02}_{-.02}$	$38.0^{+.04}_{-.04}$	$38.1^{+.08}_{-.10}$	37.7	37.4	$36.8^{+.09}_{-.11}$
68	RX J2303.9–5517	<37.1	<36.7	$37.3^{+.09}_{-.11}$	<37.5	36.4	36.4	$36.2^{+.10}_{-.13}$
69	RX J2304.6–3501	<36.6	$36.9^{+.03}_{-.03}$	$36.8^{+.05}_{-.06}$	<36.7	36.1	36.0	$35.7^{+.18}_{-.30}$
70	RX J2304.6–5128	$38.1^{+.02}_{-.02}$	$38.1^{+.02}_{-.02}$	$37.6^{+.07}_{-.09}$	<37.6	36.7	36.7	$36.2^{+.14}_{-.20}$
71	RX J2317.8–4422	$37.7^{+.10}_{-.13}$	$37.7^{+.07}_{-.09}$	$38.0^{+.05}_{-.05}$	<37.8	37.0	37.4	$36.4^{+.18}_{-.32}$
72	RX J2325.2–3236	<38.3	<38.1	$38.4^{+.08}_{-.09}$	<38.8	37.4	37.6	$36.9^{+.22}_{-.47}$
73	RX J2340.6–5329	<38.6	$38.1^{+.11}_{-.14}$	$38.7^{+.09}_{-.11}$	<38.7	37.5	37.9	$37.2^{+.27}_{-.90}$
74	MS2340.9–1511	$37.9^{+.08}_{-.09}$	<37.5	<37.8	$38.4^{+.05}_{-.06}$	37.6	38.0	$36.8^{+.14}_{-.21}$
75	RX J2349.1–3311	—	—	—	—	37.1	36.9	$36.6^{+.11}_{-.15}$
76	RX J2349.3–3125	$38.0^{+.09}_{-.12}$	$37.8^{+.05}_{-.06}$	<37.7	$38.3^{+.05}_{-.05}$	37.2	37.1	$36.7^{+.11}_{-.15}$

[1)] Errors based on the statistical uncertainties in the spectral flux at the reference energy of the power-law fits, uncertainties in $\alpha_{\rm x}$ not included

selected samples. The high mean 250 eV flux would then represent an emission component superimposed on the nuclear steep-spectrum component (i.e. a soft excess). It appears, therefore, that a disk-like BBB emission component competing with a nuclear steep-spectrum component becomes increasingly more apparent at optical and soft X-ray wavelengths as the luminosity increases.

5. Discussion

Normal Sy1 galaxies typically show a Big Blue Bump which is most pronounced in the UV (Walter et al. 1994). In the optical and soft X-ray ranges, the BBB competes with an underlying continuum which appears above keV energies with the canonical hard X-ray slope of 0.7 ($\sim$1.0 after subtraction of a reflection component) and which has a steep spectrum in the optical. Generally, a slope of $\sim$ 1.3 connects the optical and keV energy ranges. Since the optical slopes are often much steeper than 1.3, the optical and X-ray continua are not part of the same spectral component, but seem to be energetically linked. In the infrared, part of the BBB emission seems to be reprocessed by a circum-nuclear dust torus (Krolik 1996).

5.1. Soft X-ray excess or lack of hard X-rays?

In general, the steep X-ray spectra of soft X-ray selected AGN could indicate (i) an excess of soft X-rays over the canonical (flat) hard X-ray continuum (i.e. an extension of the BBB into the X-ray range) or (ii) a systematic lack of emission around 1 keV and possibly above. Several authors favored case (i) (e.g. Córdova et al. 1992, Puchnarewicz et al. 1992, Walter & Fink 1993, Boller et al. 1996), while Laor et al. (1994) argued for case (ii) based on their ROSAT PSPC observations of PG quasars. Laor et al. suggested that "a steep $\alpha_{\rm x}$ is associated with a weak hard X-ray component, relative to the near-IR (60μm) and optical emission, rather than a soft X-ray excess". Warm absorbers are also in line with case (ii) (see Sect. 5.3).

The new soft X-ray selected AGN seem to follow case (i), since the 250 eV luminosities are clearly enhanced relative to the optical and hard X-ray luminosities compared with the hard X-ray selected AGN, whereas the optical-to-1-keV spectral indices are the same (1.3) (Fig. 3, Table 2). Pointed ROSAT observations with higher statistical significance corroborate the existence of a separate hard X-ray component at least in some of our objects. Whether an underlying hard X-ray continuum indeed exists in general for soft X-ray AGN remains open[3].

5.2. $\Delta N_{\rm H}$ as a measure of the soft X-ray excess

We have seen that the intrinsic absorption is low in the soft X-ray AGN. However, the picture becomes a bit more complicated on a second view. The quantities $N_{\rm H}$ as well as $\alpha_{\rm x}$ were

[3] The soft X-ray selected Seyfert galaxy RX J1034+39 (Z 1031.7+3954), e.g., has a steep ASCA spectrum which continues up to at least 10 keV without flattening (Pounds et al. 1995).

Table 3. Means and standard errors of the means, median values, and 90% ranges. Luminosities are at rest-frame wavelengths or energies, respectively. Only the 71 soft X-ray AGN for which IRAS data were available were used. See text for treatment of upper limits in Table 2.

	soft X-ray AGN			hard X-ray AGN		
	mean	median	90% range	mean	median	90% range
$\log \nu L_{100\mu}$	37.11±0.12			36.89±0.14	36.85	36.2-37.8
$\log \nu L_{60\mu}$	37.31±0.10			36.98±0.13	36.86	36.2-37.8
$\log \nu L_{25\mu}$	37.40±0.10			37.10±0.14	36.99	36.2-37.8
$\log \nu L_{12\mu}$	37.23±0.12			37.16±0.12	37.19	36.4-37.8
$\log \nu L_{\rm V}$	37.19±0.07	37.12	36.0-38.2	37.10±0.12	36.98	36.4-37.8
$\log \nu L_{250\rm eV}$	37.17±0.08	37.10	36.0-38.2	36.68±0.16	36.77	35.6-37.4
$\log \nu L_{1\rm keV}$	36.49±0.08	36.54	35.6-37.4	36.44±0.15	36.51	35.6-37.0
$\alpha_{\rm x}$	2.11±0.10	1.96	1.3-2.7	1.35±0.06	1.40	1.0-1.7
$\alpha_{\rm opt}$	0.96±0.08	1.03	0.0-1.9	1.37±0.20	1.31	0.3-2.1
$\alpha_{\rm ox-soft}$	1.04±0.02	1.05	0.7-1.2	1.21±0.05	1.22	0.9-1.5
$\alpha_{\rm ox-hard}$	1.26±0.02	1.25	1.1-1.4	1.25±0.04	1.26	1.0-1.4
$\alpha_{60\mu-\rm opt}$	1.11±0.03			0.94±0.04	0.95	0.6-1.3
$\alpha_{60\mu-\rm soft}$	1.05±0.02			1.08±0.03	1.08	0.9-1.2
$\alpha_{60\mu-\rm hard}$	1.19±0.02			1.12±0.03	1.12	1.0-1.3
$\alpha_{12\mu-\rm opt}$	1.23±0.05			1.05±0.05	1.08	0.7-1.3
$\alpha_{12\mu-\rm soft}$	1.08±0.03			1.14±0.03	1.15	0.9-1.4
$\alpha_{12\mu-\rm hard}$	1.25±0.02			1.18±0.02	1.19	1.1-1.3
z	0.144±0.013	0.113	0.03-0.30	0.050±0.011	0.033	0.01-0.10

Table 4. Spearman rank-order correlation coefficients $r_{\rm s}$ (below diagonal) and significance levels t (above diagonal) for N = 71. Negative values denote an anti-correlation and positive values a correlation.

	$\log \nu L_{60\mu}$	$\log \nu L_{\rm V}$	$\log \nu L_{250\rm eV}$	$\alpha_{\rm x}$	$\alpha_{\rm opt}$	$\alpha_{\rm ox-soft}$	$\Delta N_{\rm H}$	rank($\alpha_{\rm x}$)−rank($\Delta N_{\rm H}$)
$\log \nu L_{60\mu}$	1	8.6	8.6	3.1	−3.2	−0.9	−1.4	2.9
$\log \nu L_{\rm V}$	0.72	1	14.0	3.8	−5.3	−0.2	−1.6	2.6
$\log \nu L_{250\rm eV}$	0.72	0.86	1	6.7	−5.3	−3.9	−2.0	4.3
$\alpha_{\rm x}$	0.35	0.42	0.63	1	−3.9	−4.7	−2.2	11.4
$\alpha_{\rm opt}$	−0.36	−0.54	−0.54	−0.42	1	0.6	3.1	−4.6
$\alpha_{\rm ox-soft}$	−0.11	0.02	−0.43	−0.49	0.07	1	1.0	−3.0
$\Delta N_{\rm H}$	−0.17	−0.19	−0.23	−0.26	0.35	0.12	1	−11.4
rank($\alpha_{\rm x}$)−rank($\Delta N_{\rm H}$)	0.33	0.30	0.46	0.81	−0.48	−0.34	−0.81	1

measured from single power-law fits. While this may be an acceptable first-order approximation, many AGN possess a soft excess over a flatter hard X-ray spectrum (see e.g. Leighly et al. 1996, Reynolds 1997, Walter et al. 1994). The result is a negative curvature over the ROSAT spectral range. The excess is then measured both by a larger $\alpha_{\rm x}$ and $N_{\rm H,fit} < N_{\rm H,gal}$ (negative $\Delta N_{\rm H}$). The slope $\alpha_{\rm x}$ is weighted towards higher energies, while $\Delta N_{\rm H}$ is most affected by the excess at the lowest energies. Therefore $\Delta N_{\rm H}$ is in principle affected both by intrinsic absorption and an excess of soft X-ray emission. Puchnarewicz et al. (1995b) discussed the case of the soft AGN RX J2248-51 with $N_{\rm H,fit} < N_{\rm H,gal}$. They showed this to be a result of a steepening of the X-ray spectrum towards lower energies rather than a 'hole' in the interstellar gas at the position of this source. RX J2248-51 is also in contained in our sample.

We find marginal evidence for a relation between $\Delta N_{\rm H}$ and $\alpha_{\rm opt}$ in the way expected if the X-ray spectra increasingly steepen towards 0.2 keV in the sources with the flattest optical spectra (Table 4). The significance of the correlation is only t = 3.1, but it is increased for the anti-correlation between

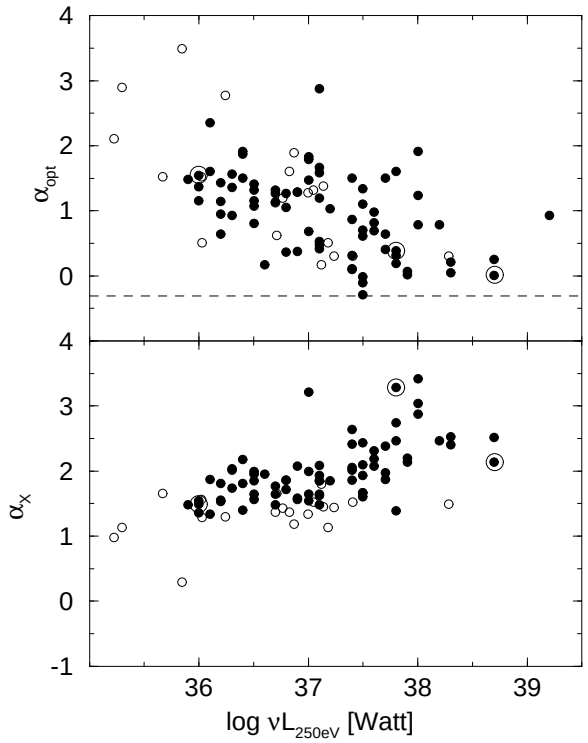

Fig. 6. Optical and X-ray spectral index vs. 250 eV luminosity. The dashed line indicates the saturation value $\alpha_{\rm opt} = -0.3$ expected for a bare accretion disk spectrum. The spectral energy distributions of the sources corresponding to the encircled points are shown in Fig. 4. The dispersion in $\alpha_{\rm opt}$ is larger than expected from the uncertainties (± 0.4, see Sect. 3.1). Solid circles denote AGN from the soft, and open circles from the hard comparison sample. WPVS007 and RX J0134-42 are off the plot ($\alpha_{\rm x}$=8.0, log $\nu L_{250\rm eV}$=36.2; 6.7, 37.5, respectively).

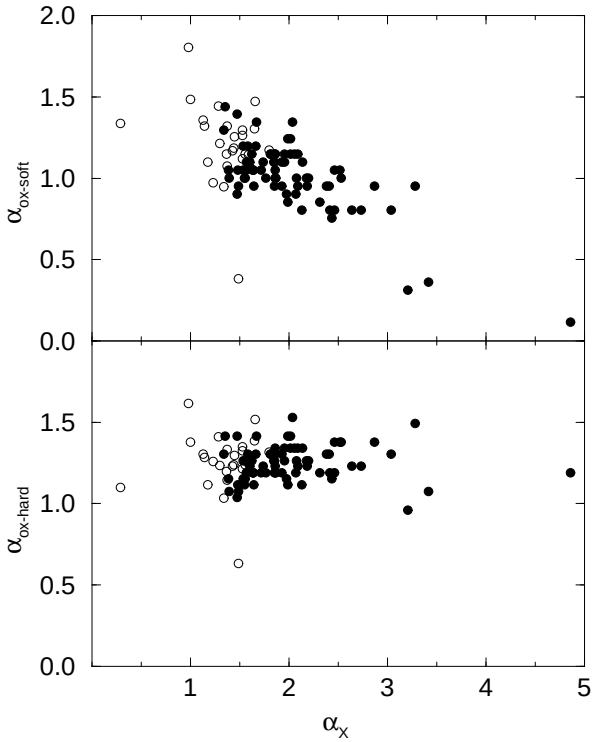

Fig. 7. Optical to X-ray spectral indices $\alpha_{\rm ox-soft}$ and $\alpha_{\rm ox-hard}$ vs. X-ray slope $\alpha_{\rm x}$. WPVS007, RX J0134-42, and RX J0136-35 are off the plot ($\alpha_{\rm x}$=8.0, $\alpha_{\rm ox-soft}$=1.2, $\alpha_{\rm ox-hard}$=2.7; 6.7, 1.2, 2.5; 4.9, 0.6, 1.2, respectively). Solid circles denote AGN from the soft and open circles from the hard comparison sample.

the combined rank [Rank($\alpha_{\rm x}$) − Rank($\Delta N_{\rm H}$)] and Rank($\alpha_{\rm opt}$), which yields $t = -4.6$. If $\Delta N_{\rm H}$ were unrelated to the soft excess, one would have expected a lower significance for the combined ranks than for the individual ones. Of course, it is difficult to find significant deviations from single power law spectra on the basis of RASS PSPC spectra alone which only contain a few hundred photons typically. Further analysis of higher signal-to-noise pointed PSPC spectra, available for some of the AGN in our sample, is required to investigate this effect in more detail.

5.3. Origin of the optical and X-ray emission components

One of our main findings is that the new soft X-ray selected AGN are Sy1 galaxies with an enhanced BBB emission component relative to the underlying continuum making the optical continuum blue and the soft X-ray spectrum steep (Fig. 4). Puchnarewicz et al. (1996) recently reported a similar $\alpha_{\rm x}$-$\alpha_{\rm opt}$ relation in the RIXOS AGN sample which supports our result. The strong correlation between $\alpha_{\rm x}$ and $\nu F_{1375\text{Å}}/\nu F_{2\rm keV}$ for Sy 1 nuclei in general (Walter & Fink 1993) is another way of presenting the same relation between the BBB and soft X-rays, and our results support their interpretation of this soft X-ray excess. Although less significant, it seems that the IR emission is also enhanced which would indeed be expected if re-processing of the BBB emission by dust is important. The extreme blueness of some of the optical spectra ($\alpha_{\rm opt}$ approaches $-1/3$) which has also been found in other AGN (Richstone & Schmidt 1980, Sun & Malkan 1989), is in agreement with emission from an optically thick, geometrically thin accretion disk.

The enormous width of the BBB requires additional comptonization of the optically thick disk spectrum by a hot corona (Matt et al. 1993) or near-Eddington accretion (Ross et al. 1992) both of which lead to copious soft X-ray production. Whether the large dispersion in the observed soft X-ray slopes represents a true dispersion in the emission process or is rather the consequence of the superposition of a (possibly Wien-shaped) ultrasoft X-ray component with a separate flatter hard X-ray component remains an open issue in the absence of hard X-ray data.

The ubiquitous $\alpha_{\rm ox-hard} \simeq 1.3$ argues for a common origin of the steep-spectrum optical emission component and the hard X-ray component[4]. In some AGN the optical spectrum is steeper than the optical-to-X-ray spectrum which is inconsistent with a single non-thermal continuum unless there is reddening in these sources. We have no evidence, however, for systematic reddening effects from our low-resolution identification spectra.

[4] A correlation $L_{\rm opt} \propto L_{\rm x}$ seems to hold for AGN in general (La Franca et al. 1995).

An optical continuum component which does not connect as a power law with the hard X-ray part of the spectrum, but is still energetically coupled to the hard X-ray emission component, could result from thermal re-processing of the hard X-rays by cold matter. The cold matter intercepting hard X-rays may be located in the outer accretion disk (Collin-Souffrin 1987). In order to re-process a large fraction of the hard X-ray power, the solid angle subtended by the disk with respect to the hard X-ray source must be large. A plausible geometry would be that the hard X-ray source is located *above* a geometrically thin disk at a height comparable to the optical emission radii of the disk $\sim 10^2 - 10^4 R_{\rm G}$ where $R_{\rm G} = 2GM/c^2$ denotes the Schwarzschild radius. This geometry is in rough agreement with the one found by Clavel et al. (1992) from multi-wavelength variability studies of the hard X-ray AGN NGC 5548 from which a height of $\sim 100 R_{\rm G}$ was inferred.

The predominance of the BBB appears to increase with the observed soft X-ray luminosity which, in turn, depends on the accretion rate and on the viewing angle. A variation of black hole mass keeping $\dot{M}/M \propto \dot{M}/\dot{M}_{\rm Edd}$ constant does not seem to be responsible for the variable bump strength. With increasing luminosity, the inner disk temperature would decrease according to $T_* \propto M^{-\frac{1}{4}}$ and would, therefore, fail to explain the observed soft X-ray excess unless the effect is compensated by comptonization (e.g., Czerny & Elvis 1987). Also, the variability time scales would be expected to increase with luminosity which does not seem to be the case. This effect would be quite dramatic, since the most luminous AGN in our sample would require black hole masses a factor of $\sim$100 higher than in the weakest sources.

It is more likely that the effect is due to an increasing $\dot{M}/\dot{M}_{\rm Edd}$ and that the most luminous soft X-ray selected AGN are close to Eddington accretion. The soft X-ray excess would be related to the inner disk temperature increasing as $T_* \propto \dot{M}^{\frac{1}{4}}$. There would be a striking analogy between AGN and Galactic Black Hole candidates such as Cyg X-1 (Pounds et al. 1995) which display 'high' states with a thermally dominated UV/soft X-ray spectrum at a near-Eddington accretion rate and 'low' states in which the hard X-rays are much more pronounced and the accretion rate is reduced. RX J0134-42 has indeed shown a turn-on of the hard X-ray component with an associated decrease in the strength of the BBB (Mannheim et al. 1996). Also the transient sources WPVS007 (Grupe et al. 1995b) and IC3599 (Brandt et al. 1995, Grupe et al. 1995a) may fit into this picture. In fact, any transient Eddington high state produced by a $\gtrsim 10^6 M_\odot$ black hole would be located to the right of $\log L_{\rm x} \simeq \log L_{250{\rm eV}} \approx 37$ in Fig. 6 and could be responsible for the large dispersion in $\alpha_{\rm x}$.

Further support for the high state scenario may come from the emission line properties of the soft AGN (which we will describe in more detail in Paper II). There exists a relation between $\alpha_{\rm x}$ and FW(Hβ) in the sense that steep X-ray spectra are observed preferentially in systems with narrow permitted lines (Boller et al. 1996, Paper II). Boller et al. argue that narrow-line Sy1s have moderate black hole masses in the range $\sim 10^6 - 10^7 M_\odot$ but accretion rates $\dot{M}/M$ higher than in normal Sy1s. The enhanced photoionizing flux destroys the emission line clouds closest to the central black hole.

Alternative explanations of the $\alpha_{\rm x}$-FW(Hβ) relation do not seem to be consistent with our results. If the emission line clouds originate in a torus geometry, the smallest line widths would be expected for a face-on orientation, i.e. the relation would be a mere orientation effect. There would be no absorbing cold gas and therefore steep X-ray spectra and blue optical continua. With increasing viewing angle, one would expect a hardening of the X-ray spectra owing to absorption by the gaseous torus. However, intrinsic absorption by cold gas is not responsible for the slopes of the X-ray spectra. Absorption by warm dust reddening the optical spectra and steepening the X-ray spectra would have the opposite effect of what is needed. The soft AGN could also correspond to relativistic accretion disks seen near the disk plane where the X-ray (but not the optical) flux is Doppler enhanced. Unless the emission line gas is moving preferentially perpendicular to the disk (e.g., a disk wind), there is, however, no reason to expect smaller line widths in these AGN. While it is clear that the soft X-rays are not viewed through a dusty torus with large column density, it is not possible to further constrain the geometry and inclination based on the continuum properties alone.

It is undisputed that the large range of luminosities in AGN generally requires a range in black hole masses, but it appears plausible that the peculiar properties of the soft X-ray selected Seyferts are due to a temporarily increased $\dot{M}$ for a rather narrow range in M.

5.4. Warm absorbers

A primary X-ray spectrum could appear steeper in the soft X-ray band than the original spectrum if it is absorbed by partially ionized matter at intermediate energies between $\sim$0.5 and 3 keV, which becomes optically thin for soft X-rays below 0.5 keV. Netzer (1993) has shown that the deep edges are practically washed out in realistic models for the geometry of a warm absorber taking into account emission lines and reflection. Several observations, such as the ROSAT observations of IRAS 13349+2438 (Brandt et al. 1996) or the 3C351 observations of Fiore et al. (1993), have led to claims that this warm absorption could be important in mimicking a soft excess (see also Komossa & Fink 1997). With ASCA, evidence for warm absorbers in AGN has been found in the form of the OVI, OVII, and OVIII absorption edges (e.g. George et al. 1995, Mihara et al. 1995, Otani et al. 1996) without, however, obliterating the need for primary X-ray spectra steeper than the canonical hard X-ray spectra. The spectral steepening is maximized if much of the absorber is optically thin to radiation below the K- and L-edges of the more abundant elements, causing the spectrum to be selectively depressed around 1 keV. Although warm absorbers are present in some of the soft X-ray emitting AGN (see Brandt et al. 1996, we will also discuss this issue on the polarized AGN of our sample in two separate papers, Grupe et al. 1997 and Wills et al. in prep.), there is no evidence on the average for an association of steep spectra and low 1 keV

fluxes ($\alpha_{\rm ox-hard}$ = const.). Therefore, warm absorbers cannot be the primary cause for the very soft X-ray spectra of our soft sample.

6. Conclusion

The interpretation of the BBB emission component in AGN in terms of an accretion disk has generally suffered from the presence of additional optical and hard X-ray emission components radiating comparable amounts of energy. Our data demonstrate that soft X-ray selection provides a powerful means for discovering AGN with almost bare BBB emission characterized by blue optical spectra with a slope approaching $\alpha_{\rm opt} \approx -1/3$ and very soft X-ray spectra. We speculate that these very soft X-ray AGN correspond to $10^6 - 10^7 M_{\odot}$ black holes in a high state with near-Eddington accretion. The phenomenon is likely to be of a transient nature, basically similar to what has been observed in IC3599, WPVS007, and RXJ0134-42, although on longer time scales. Further studies in the UV and EUV bands are required to measure the shape and variability of the BBB in the wavelength regime where most of the bolometric luminosity is apparently released. It is also important to clarify the role of absorption by warm dust, the nature of the underlying continuum, and its connection to the BBB by additional hard X-ray and near-infrared observations.

Acknowledgements. We thank B. Wills and the anonymous referee for useful comments. We are also grateful to assistance by the ROSAT team at the MPE. We used the NASA/IPAC Extragalactic Database which is operated by the Jet Propulsion Laboratory, Caltech, under contract with the National Aeronautics and Space Administration, and IRAS data provided by the Infrared Processing and Analysis Center, Caltech. This research was initially supported by the DARA grant 50 OR 92 10 and later on by the Bundesanstalt für Arbeit.

References

Arnaud K.A., Branduardi-Raymond G., Culhane J.L. et al. 1985, MNRAS 217, 105
Babu G.J., & Feigelson E.D. 1996, Astrostatistics. Chapman & Hall, London, Chapter 10
Band D.L., Malkan M.A. 1989, ApJ 345, 122
Barvainis R. 1993, ApJ 412, 513
Boller Th., Trümper J., Molendi S.al. 1993, A&A 279, 53
Boller Th., Brandt W.N., Fink. H.H. 1996, A&A 305, 53
Brandt W.N., Pounds K.A., Fink H.H., Fabian A.C. 1995, MNRAS 273, L47
Brandt W.N., Fabian A.C., Pounds K.A. 1996, MNRAS 278, 326
Clavel J., Nandra K., Makino F. et al. 1992, ApJ 393, 113
Collin-Souffrin S. 1987, A&A 179, 60
Córdova F.A., Kartje J.F., Thompson R.J. et al. 1992, ApJS 81, 661
Czerny B., Elvis M. 1987, ApJ 321, 305
Dickey J.M., Lockman F.J. 1990, ARA&A 28, 215
Ferland G.J., Rees M.J. 1988, ApJ 326, 889
Fiore F., Elvis M., Mathur S., Wilkes B.J., McDowell J.C., 1993, ApJ 415, 129
George I.M., Turner T.J., Netzer H. 1995, ApJ 438, L67
Grupe D., Beuermann K., Mannheim K. et al. 1995a, A&A 299, L5
Grupe D., Beuermann K., Mannheim K. et al. 1995b, A&A 300, L21
Grupe D. 1996, PhD Thesis, Göttingen University (http:/www.uni-sw.gwdg.de/preprints)
Grupe D., Wills B.J., Wills D., Beuermann K., 1997, A&A submitted
Guilbert P.W., Rees M. J. 1988, MNRAS 233, 475
Komossa S., Fink H.H. 1997, A&A 322, 719
Krolik J.H. 1996, Vistas in Astronomy 40, 9
La Franca F., Franceschini A., Christiani S. et al. 1995, A&A 299, L19
Laor A., Netzer H. 1989, MNRAS 238, 897
Laor A., Fiore F., Elvis M. et al. 1994, ApJ 435, 611
Laor A., Fiore F., Elvis M. et al. 1997, ApJ 477, 93L
Leighly K.M., Mushotzky R.F., Yaqoob T., Kunieda H., Edelson R. 1996, ApJ 469, 147
Malkan M.A., Sargent W.L.W. 1982, ApJ 254, 22
Malkan M.A. 1983, ApJ 268, 582
Mannheim K., Schulte M., Rachen J. 1995, A&A 303, L41
Mannheim K., Grupe D., Beuermann K. et al. 1996, *Proc. 'Röntgenstrahlung from the Universe'*, eds. H.U. Zimmermann, J. Trümper, and H. Yorke, MPE Report 263, p. 471
Matt G., Fabian A.C., Ross R.R. 1993, MNRAS 264, 839
Mihara T., Matsuoka M., Mushotzky R.F. et al. 1995, PASJ 46, L137
Netzer H. 1993, ApJ 411, 594
Otani C., Kii T., Reynolds C.S. et al. 1996, PASJ 48, 211
Pfeffermann E., Briel U.G., Hippmann H. et al. 1986, SPIE 733, 519
Pounds K.A., Done C., Osborne J.P. 1995, MNRAS 277, L5
Puchnarewicz E.M., Mason K.O., Córdova F.A. 1992, MNRAS 256, 589
Puchnarewicz E.M., Mason K.O., Siemiginowska A., Pounds K.A. 1995a, MNRAS 276, 20
Puchnarewicz E.M., Branduardi-Raymond G., Mason K.O., Sekiguchi K. 1995b, MNRAS 276, 1281
Puchnarewicz E.M., Mason K.O., Romero-Colmenero E. et al. 1996, MNRAS 281, 1243
Reynolds C.S., 1997, MNRAS 286, 513
Richstone D.O., Schmidt M. 1980, ApJ 235, 361
Ross R.R., Fabian A.C., Mineshige S. 1992, MNRAS 258, 189
Rush B., Malkan M.A., Fink H.H., Voges W. 1996, ApJ 471, 190
Schartel N., Walter R., Fink H. H., Trümper J. 1996, A&A 307, 33
Shields G.A. 1978, Nature 272, 706
Sun W.H., Malkan M.A. 1989, ApJ 346, 68
Thompson R.J., Puchnarewicz E.M., Córdova F.A., Mason K.O. 1994, ApJ 420, 136
Voges W. 1997, Proc. 5th Int. Workshop on *Data Analysis in Astronomy*, World Sci. Publ. Corp., in press
Voges W., Boller T., Dennerl K. et al. 1996, in: *Proc. 'Röntgenstrahlung from the Universe'*, eds. H.U. Zimmermann, J. Trümper, and H. Yorke, MPE Report 263, p. 637
Voges W., Aschenbach. B., Boller Th. et al. 1997, A&AS submitted
Walter R., Fink H.H. 1993, A&A 274, 105
Walter R., Orr A., Courvoisier T.J.L. et al. 1994, A&A 285, 119
Zimmermann H.U., Becker W., Belloni S., et al., 1994, EXSAS User's Guide, MPE Report 257

This article was processed by the author using Springer-Verlag LaTeX A&A style file *L-AA* version 3.